Pergamon

Int. J. Heat Mass Transfer. Vol. 38, No. 11, pp. 2075–2088, 1995

0017–9310/95 $9.50 + 0.00

0017–9310(94)00319–X

Forces on bubbles growing and detaching in flow along a vertical wall

W. G. J. VAN HELDEN, C. W. M. VAN DER GELD† and P. G. M. BOOT

Eindhoven University of Technology, Faculty of Mechanical Engineering, W-hoog 3.144, P.O. Box 513, 5600 MB Eindhoven, The Netherlands

(*Received* 22 *June* 1994 *and in final form* 14 *September* 1994)

Abstract—Experiments are performed on bubble detachment from an artificial cavity in a plane wall of a vertical rectangular channel. Mean upward velocity is varied. Steam bubbles are generated by local heating of the cavity, nitrogen bubbles of about the same size by injection. The experiments show a difference in take off direction between vapor and nitrogen bubbles. Steam bubbles take off into the liquid, while nitrogen bubbles more or less slide parallel to the wall. The bubble detachment radius decreases for increasing bulk liquid velocity, in a way that merely depends on the detachment radius without convection. Nitrogen bubbles, coming from a capillary with approximately the same radius are larger than water vapor bubbles. A force coefficient fit is performed on force components perpendicular to the wall. By analyzing flow- and non-flow experiments separately, some of the forces are quantified. By combining the results of nitrogen bubble and steam bubble experiments, a force due to the temperature difference at the bubble foot is studied. Such a force could explain the observed differences between steam and nitrogen bubbles. It is found that either a vorticity lift force of the type found by Auton [The dynamics of bubbles, drops and particles in motion in liquids, Ph.D. thesis, University of Cambridge (1983)] is negligible, or this temperature difference force may be important. A commonly used criterion to predict detachment radii is found not to be satisfactory.

1. INTRODUCTION

As boiling heat transfer occurs frequently in various industrial processes, fundamental knowledge of bubble growth and detachment from heated surfaces is important. Better knowledge may help to improve efficiency and reliability of boiling processes.

In many industrial applications boiling takes place in vertical pipes. However, most experiments on bubble detachment were performed on horizontal surfaces. Gravity then plays an important, if not dominant, role. Bubbles are nonetheless reported to detach against gravity from downward facing plates or from heated wires [2]; even in microgravity, bubbles detach as a result of self-induced convection [3]. Clearly, detachment without the action of gravity occurs, as is further discussed below.

Siegel [2] studied boiling heat transfer in gravity, reduced to as low as 0.001 g. At low g, bubbles were found to detach relatively slowly, resulting in coalescence of subsequent bubbles. Growth rate and detachment diameter increased with decreasing g. Siegel still considered buoyancy as the main cause of bubble detachment.

Cooper and Chandratilleke [3] observed bubbles detaching from a horizontal, upward faced surface in n-hexane in a known temperature gradient. In their experiments they reduced the gravitational acceleration to about 0.4% of Earth gravity. In microgravity, bubble shape and departure were explained with the aid of the fully developed temperature boundary layer and wall superheating, without buoyancy. In microgravity this thermal boundary layer was found to have a dominating effect on growth and departure [3]. Detachment 'against' gravity was found to be stimulated by strong subcooling of the liquid and by a thin thermal boundary layer.

In the present study, bubbles detach at ambient pressure from an artificial cavity in a vertical plane wall under 1 g and the importance of gravity and other forces in these circumstances is investigated. Some of these forces are due to interfacial stresses created by liquid flowing upward along the wall.

For instance the effect of convection on bubble detachment was investigated by Koumoutsos *et al.* [4]. They studied bubbles detaching from a horizontal wall and found the detachment diameter to decrease with increasing liquid velocity. Al-Hayes and Winterton [5] studied gas bubbles taking off into a flowing liquid. The inclination of their test tube was varied between -30 and $+30^{\circ}$ from the horizontal. Their interpretation was based on the combined action of buoyancy, surface tension and drag forces. Detachment diameters were reproduced reasonably well. However, a maximum detachment diameter was predicted to occur with increasing downward flow, which was not observed experimentally.

Cooper *et al.* [6] performed a series of measurements on growing bubbles in supersaturated n-hexane, with and without gravity, in fully developed

† Author to whom correspondence should be addressed.

NOMENCLATURE

A	area of cross section
c	specific heat
C	constant coefficient
C_g	growth constant
D	diameter
E	constant
e	unit vector
F	force
g	gravity acceleration
h	enthalpy of evaporation
H	height
H_0	distance from bubble top to capillary axis
k	heat transfer coefficient
l	width of channel
m	mass
P	pressure
q	heat flux
Q	heat flow rate
R	radius
Re	Reynolds number
T	temperature
u	velocity in x-direction
V, v	velocity in y-direction
$\forall$	volume
V^*	friction velocity.

Greek symbols

α	thermal diffusivity
β	contact angle
γ	growth exponent
δ	boundary layer thickness
θ	dimensionless temperature
ν	kinematic viscosity
ξ	exponent
ρ	mass density
σ	surface tension
τ	shear stress
ϕ	circumferential angle
Φ	take-off angle
ω	vorticity.

Subscripts

a	advancing, upstream
b	bubble
bulk	liquid bulk
B	buoyancy
cap	capillary
m	bubble midpoint
n	net, total
d	at detachment
D	drag
e	expansion
g	gas–vapor
H	hydraulic
l	liquid
L	lift
r	receding, downstream
rel	relative
sat	at saturation
top	at bubble top
w	wall
x,y	x-, y-direction
∞	at infinity, undisturbed.

Superscripts

$\overline{}$	mean.

laminar flow. At 1 g, bubbles were found to slide along the vertical wall, forming a microlayer at the bubble foot. The drag force on these bubbles was found to be larger than for unbounded bubbles. Viscous forces in the microlayer wedge were held responsible for this. From measurements under microgravity they concluded that bubble growth is merely dependent on the Jakob number [defined as $\rho_l c(T-T_{sat})/(\rho_g h)$] and liquid thermal diffusivity, with negligible influence of viscosity and surface tension.

More recently, Klausner *et al.* [7] studied the detachment of bubbles from a horizontal heated wall into saturated flowing R113. Their heater was a NiCr strip without artificial cavities. They found the majority of the bubbles first to move parallel to the wall with their foot still at the wall before lifting off. Because no fixed nucleation site was studied, their results were stated in terms of probability density functions. An increase of wall heat flux or a decrease of liquid mass flux was found to cause a shift of the mean detachment diameter towards larger values. From a force balance, this result was predicted with main parameters being the liquid velocity and the wall superheat. Of main importance in their force balance parallel to the wall was the force resulting from asymmetrical bubble growth. The same force balance was used by Zeng *et al.* [8] to predict bubble detachment diameters in the horizontal flow boiling of R113. In the present study, the importance of the asymmetrical bubble growth is re-evaluated.

From the foregoing it is concluded that in situations where buoyancy is relatively unimportant, the effect of wall superheating may be important in bubble detachment. The relative importance of induced temperature gradients is expected to be large in the case of bubbles detaching perpendicular to a vertical wall, since buoyancy in this case is mainly active parallel. In the present study the importance of forces resulting from temperature gradients is examined. To this end the actions of forced convection and heat transfer are disentangled by means of dedicated experiments.

2. EXPERIMENTAL

Experiments are performed in a loop mainly comprising stainless steel piping with 40 mm inner diameter. See the schematic of Fig. 1.

Water is pumped around and heated electrically to saturation temperature. The water then passes the test section with a square cross section of 20×20 mm^2 (Fig. 2) and subsequently the condensor. The distance from round–square transition at the test section entrance to the bubble generation site is approximately 50 cm. For the liquid flow rates employed this is long enough to guarantee a fully developed flow along the bubbles. The channel Reynolds number in the experiments is varied between 11 000 and 58 000. As the condensor is open to atmospheric pressure, the static pressure at the bubble generation site is roughly equal to the sum of atmospheric pressure and the water head above the bubble generator. The dissolved air is removed by boiling the water several hours prior to measurement. Then the flow is set to the desired value and the heater power is changed step by step until the liquid bulk temperature is stable and as near as possible to the saturation value. The bulk liquid superheat at the bubble generator position was always less than 2K.

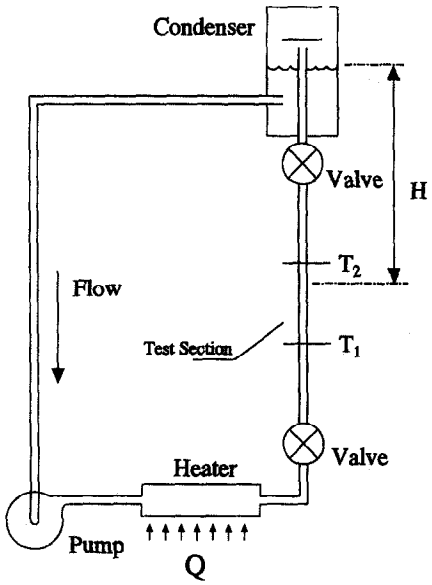

Fig. 1. Schematics of the test loop with its main components.

Bubbles are generated in the test section (Fig. 2) with the aid of a special, flush-mounted bubble generator. Two parallel glass panels allow the filming of bubble growth and take-off. The inner sides of the test section walls are polished smoothly to minimise the number of unwanted nucleation sites. Surface roughness is of the order of 15 μm.

Two types of bubble generators are employed:

- The bubble generator of type I (Fig. 3) consists of a capillary in a glass rod that is cast in a stainless steel plug. This plug is flush mounted in the test section wall and leaves a slit of less than 15 μm. The capillary mouth serves as an artificial nucleation site. Bubble generation is stimulated by heating of the capillary by means of a miniature coil inserted at the back of the capillary. The distance between electrical heating coil and bubble nucleation site is approximately 1.5 mm. The temperature of the heating coil is measured by a copper–constantane thermocouple in the centre of the coil (accuracy 2K).
- The type II bubble generator forms nitrogen bubbles by direct injection of nitrogen gas through a glass capillary. Identical plugs are used for type I and type II generators in order to create the same experimental conditions for nitrogen and steam bubbles.

The process of bubble growth and detachment is recorded by a high speed camera (Hitachi 16-DS) operated at a speed up to 5500 frames per second. Individual pictures are analyzed with the aid of a motion analyzer. Bubble contour and position coor-

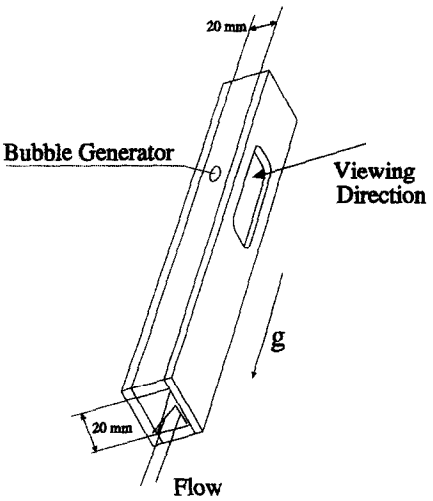

Fig. 2. Schematic view of the test section.

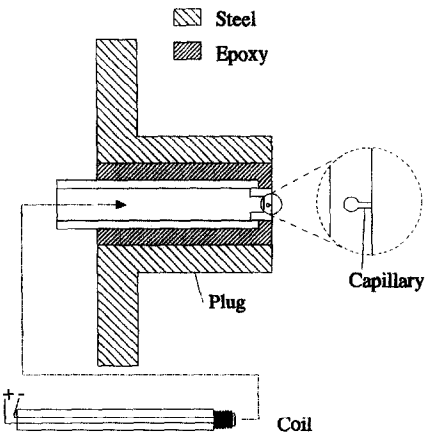

Fig. 3. Cross-section of type I bubble generator. The left side is the back of the generator, not in contact with the flow.

Table 1. Results for the vapor bubble experiments, arranged in order of increasing liquid bulk speed. T_{coil} is the heating coil temperature, $\overline{R_d}$ is the mean detachment radius. The uncertainty value is the standard deviation. $\overline{C_\gamma}$ and $\bar{\gamma}$ are determined from $R(t) = R_0 + C_\gamma t^\gamma$

Experiment no.	V_{bulk} (mm s^{-1})	T_{coil} (°C)	$\overline{R_d}$ (mm)	$\overline{C_\gamma}$ (m s$^{-\gamma}$)	$\bar{\gamma}$
N33	160	—	0.558±0.006	0.0054	1.0
N35	180	240	0.504±0.007	0.0004	1.5
N36	260	240	0.40±0.01	0.00013	1.4
N03	530	150	0.28±0.01	0.052	1.1
N07	520	220	0.282±0.006	0.07	1.2
N04	530	340	0.30±0.01	0.023	1.0
N01	660	150	0.255±0.006	0.093	1.3
N05	650	230	0.25±0.02	0.066	1.4
N08	660	340	0.25±0.04	0.0089	1.0
N27	700	—	0.21±0.03	0.04	1.2
N32	770	—	0.2±0.02	0.042	1.3
N06	840	220	0.19±0.01	0.54	1.4
N09	850	280	0.18±0.01	0.28	1.2
N02	850	340	0.21±0.02	0.04	1.0

dinates are fed into a computer and coupled to time as determined with the aid of timing dots produced by a stroboscope (accuracy 0.25 ms). The positioning accuracy of the hairlines of the analyzer in combination with the total magnification leads to a coordinate accuracy of 30 μm, approximately.

With vapor bubbles, a bubble generator with a capillary of 130 μm diameter is used. The water bulk speed is varied from 160 to 850 mm s^{-1} (accuracy 10 mm s^{-1} as measured by a rotameter), the heating coil temperature from 150 to 340°C. Nitrogen bubble experiments are performed in the same velocity range, with capillaries of 96, 101 and 132 μm diameter.

3. EXPERIMENTAL RESULTS

Table 1 lists the values found for the mean detachment radius in boiling. These are averages of 7–10 bubbles of a cine film recording of an experiment. Because the heating of the coil generator is indirect, only an estimate of the local temperature can be given. To determine the growth rate of individual bubbles, the attached bubble is assumed to have the shape of a truncated sphere, as depicted in Fig. 9. Its radius as a function of time is written as:

$$R = R_0 + C_\gamma \cdot t^\gamma \tag{1}$$

with R_0 a constant of the order of the capillary radius, t the time, C_γ the growth constant and γ the growth exponent, the three coefficients R_0, C_γ and γ are found by applying a least-squares fit to the measured bubble radius. The mean values of C_γ and γ over a series of bubbles in one experiment are calculated and listed in Tables 1 and 2.

Figure 4 shows relative bubble midpoint positions after detachment for both types of generators. The x- and y-positions of the bubble midpoint are relative to the midpoint position at the moment of detachment. Steam bubbles are apparently launched into the liquid resulting in a detachment direction closer to the normal. Nitrogen bubbles, on the other hand, slide along the wall. This observation marks the difference between the heated and the isothermal cases. The trajectories of Fig. 5 are obtained by applying a least-squares polynomial fit to the trajectory data of a complete set of bubbles from one experiment. Clearly the

Table 2. Mean detachment radius found for nitrogen bubbles. Three series with different capillary radius are shown

Experiment no.	R_{cap} μm	V_{bulk} (mm s^{-1})	$\overline{R_d}$ (mm)	$\overline{C_\gamma}$ (m s$^{-\gamma}$)	$\bar{\gamma}$
N31	48	130	0.32±0.01	0.002	0.46
N30	48	700	0.25±0.01	0.015	0.63
N62	50	0	1.248±0.004	0.009	0.46
N60	50	570	0.55±0.02	0.039	0.66
N61	50	900	0.40±0.02	0.083	0.75
N68	66	0	1.654±0.002	0.013	0.49
N65	66	540	0.78±0.02	0.049	0.69
N66	66	720	0.65±0.02	0.080	0.75
N67	66	980	0.52±0.02	0.213	0.88

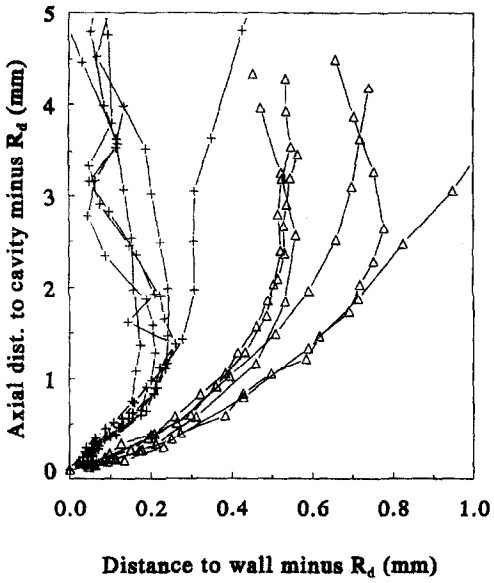

Fig. 4. Trajectories of bubble midpoints after detachment, relative to the bubble midpoint at detachment. (△) water vapor bubbles from experiment N01 (Table 1); (+) nitrogen bubbles from experiment N30 (Table 2). Note that the x- and y-axis are differently scaled.

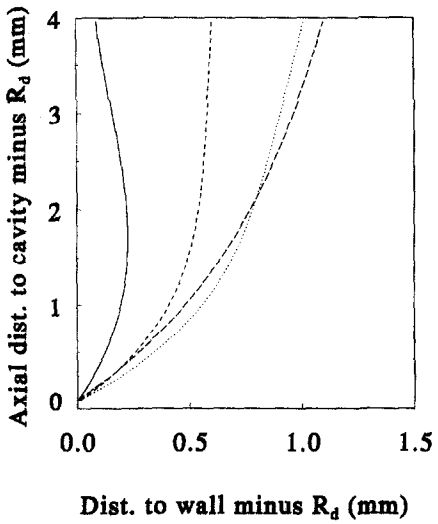

Fig. 5. Mean trajectories of relative bubble midpoint positions from four experiments. Solid line: nitrogen bubbles (N30). The other three lines are steam bubble trajectories: short dash, N01 (T_{coil} = 150°C); long dash, N05 (230°C); dots, N08 (340°C).

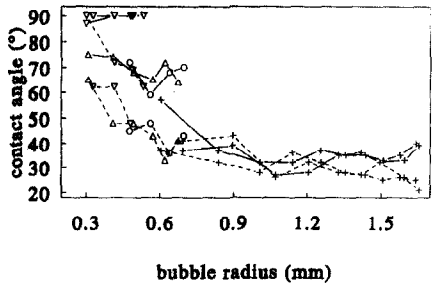

Fig. 6. β_a (solid lines) and β_r (dashed lines), for nitrogen bubbles (D_{cap} = 132μm). (+) V_{bulk} = 0 m s^{-1}; (△) 0.54 m s^{-1}; (○) 0.72 m s^{-1}; (▽) 0.98 m s^{-1}.

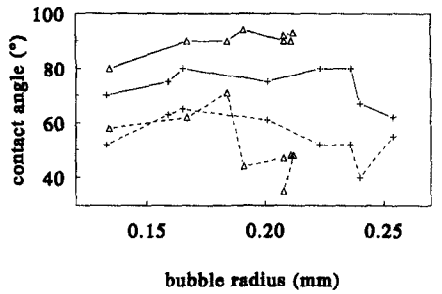

Fig. 7. β_a (solid lines), and β_r (dashed lines), for two steam bubbles. (+) V_{bulk} = 0.65 m s^{-1}; (△) 0.7 m s^{-1}.

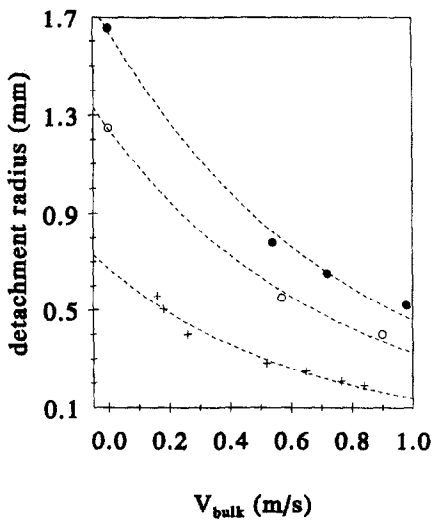

Fig. 8. Mean bubble detachment radius plotted as function of liquid bulk speed. Water vapor: (+) D_{cap} = 130 μm. Nitrogen: (○) D_{cap} = 101 μm; (●) D_{cap} = 132 μm. Values of water vapor bubbles are given in Table 1, those of nitrogen bubbles in Table 2.

water vapor bubble take off direction is more towards the normal than for nitrogen bubbles, while the take off angle (relative to the tangent to the wall) is slightly increased for increasing wall temperature.

For several individual bubbles, the advancing and receding contact angles are determined as a function of the bubble radius. These angles are defined in Fig. 9. Generally, the advancing contact angle exceeds the receding angle. In case of nitrogen bubbles (Fig. 6), both β_a and β_r decrease for increasing bubble radius. However, for steam bubbles β_a is constant or slightly increasing, while β_r decreases (Fig. 7).

The effect of liquid bulk velocity on bubble detachment radius is depicted in Fig. 8. The figure shows an inverse relation between detachment radius and liquid velocity. It is seen that, over the complete velocity

Table 3. Values for coefficients E_1 and E_2 that describe the relation between R_d and V_{bulk}

Set	Coefficient E_1	E_2
N_2, $D_{cap} = 101$ μm	1.24 ± 0.04	1.3 ± 0.1
N_2, $D_{cap} = 132$ μm	1.64 ± 0.05	1.28 ± 0.08
Steam, $D_{cap} = 130$ μm	0.67 ± 0.03	1.6 ± 0.1

Table 4. Angle of midpoint motion just before detachment (Φ) for the vapor bubble experiments (0° if normal to the wall and 90° if parallel to the wall)

Experiment no.	V_{bulk} (mm s^{-1})	T_{coil} (°C)	Φ (°)
N03	530	150	58 ± 3
N07	520	230	62 ± 3
N04	530	340	58 ± 3
N01	660	150	61 ± 8
N05	650	230	56 ± 2
N08	660	340	50 ± 2
N06	840	220	60 ± 3
N09	850	280	52 ± 1
N02	850	340	58 ± 2

range, vapor bubbles are smaller than nitrogen bubbles if they come from capillaries of comparable size. The detachment radius for a given capillary is written as an exponential function of bulk liquid speed:

$$R_d = E_1 \exp(-E_2 \cdot V_{bulk}). \quad (2)$$

E_1 denotes the detachment radius at zero liquid speed. Values of E_1 and E_2 are listed in Table 3.

As discussed above, vapor bubbles detach in a direction away from the wall. From the coordinates of the bubble midpoint at the first three pictures before detachment, the slope of the midpoint motion is determined by fitting a polynomial. The angle of detachment is defined to amount 0° if normal to the wall and 90° if parallel to the wall. The average angle of vapor bubbles of an experiment is tabulated in Table 4. Rather surprisingly, the angle is nearly constant for the whole range of experiments, i.e. independent of liquid velocity. Obviously the influence of increasing drag force with increasing liquid velocity is dominated by some other mechanism. In the following it is attempted to establish the importance of this mechanism. Variation of the liquid bulk speed influences the hydrodynamic forces, but also the heat exchange rate from wall to fluid. This combined effect is accounted for in the analysis. It is noted that aspect ratios (ratio of bubble axis in y-direction to that in x-direction) between 0.8 and 1.25 are measured for both nitrogen and steam bubbles. Thus the trajectory differences cannot be explained by differences in shape.

4. THE FORCES ON A DETACHING BUBBLE

It is observed above that the detachment behaviour of steam bubbles differs from that of nitrogen bubbles. In this section all forces that can be important in the detachment process are discussed. Expressions and coefficients for the forces are introduced, which will be determined further in the next section. The coordinate axes are depicted in Fig. 9.

The lift force comprises all hydrodynamic forces acting in the direction transverse to the flow. It is partly generated by the suction on an adhering body of a uniform flow over the body ('Bernoulli suction'), partly by the action of the vorticity in the approaching liquid flow:

$$\mathbf{F}_L = C_{L_1} \frac{R_{cap}}{R} A_2^1 \rho_l V_m^2 \mathbf{e}_x + C_{L_2} \rho_l \mathcal{V}_b |\mathbf{v}_{rel} \times \boldsymbol{\omega}| \mathbf{e}_x. \quad (3)$$

C_{L_1} accounts for the 'Bernoulli suction', A is the area of the bubble cross section perpendicular to the flow, R_{cap} is the capillary radius, R the bubble radius, ρ_l is the fluid density, $\mathcal{V}_b$ the bubble volume, V_m the fluid velocity at the bubble midpoint, $\mathbf{e}_x$ the unit vector in x-direction, C_{L_2} a constant and $\mathbf{v}_{rel}$ the relative velocity of fluid with respect to the bubble.

C_{L_1} is computed using Bernoulli's equation and potential flow theory. This simplification is allowed since the bubble Reynolds number is high (typically 400 for the lowest velocities), which also justifies the neglect of Saffman's lift force [9]. The computation yields $C_{L_1} = 11/8$ for the initial hemispherical bubble, with $A = \frac{1}{2}\pi R_{cap}^2$ (see Appendix A). If the bubble is growing and takes on the form of a truncated sphere, the value of this force is assumed to decrease inversely proportional to the bubble radius, in order to account for the liquid flow between the bubble and the wall. This is made explicit by the factor R_{cap}/R in equation (3).

The second lift force contribution can also be estimated from potential flow theory. Auton [1] derived the value of C_{L_2} for a bubble in an unbounded flow with small shear rate:

$$C_{L_2} = 0.53. \quad (4)$$

In the detachment of a bubble from a plane wall, the

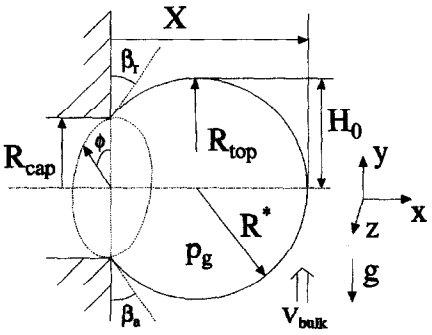

Fig. 9. Geometry used in modeling the forces acting on the bubble. Water is flowing in the positive y-direction.

vorticity ω can be approximated by the ratio of liquid velocity at the bubble cap and the bubble cap x-position (see Fig. 9): $\omega \approx v(X)/X$. The relative velocity, v_{rel}, is the water velocity at the bubble centre, V_m.

The shear rate is defined as $\omega R_b/V_{bulk}$ and should be small to justify the use of equations (3) and (4). In our situation, the assumption of a small shear rate would lead to the demand of R_b being smaller than the velocity turbulent boundary layer thickness δ, since $\omega \approx V_{bulk}/\delta$. From ref. [10] this thickness is estimated for a channel Reynolds number of 4.2×10^4 to be ≈ 5 mm in our setup. However, this is a global demand and especially near the wall the vorticity is much higher. Small bubbles will therefore experience a higher shear rate. This, combined with the fact that the flow in our situation is not unbounded, should cause a different value of C_{L_∞}.

The surface tension force in two directions is given by:

$$\mathbf{F}_\sigma = -R_{cap}\sigma \int_0^{2\pi} \sin\beta \, d\phi \mathbf{e}_x - R_{cap}\sigma \int_0^{2\pi} \cos\beta \cos\phi \, d\phi \mathbf{e}_y. \quad (5)$$

R_{cap} is the capillary radius, σ the surface tension, $\beta = \beta(\phi)$ the contact angle between the liquid–vapor interface and the wall and ϕ is the circumferential angle along the capillary mouth (see Fig. 9).

The bubble shape is assumed to approximate a truncated sphere. From the experiments it was found that β varied between 90° upstream and 43° downstream of the bubble. Values of β for intermediate ϕ are calculated assuming that β is a linear function of ϕ. A higher order fit does not lead to more accurate results. The integrals in equation (5) are then evaluated analytically. A deviation from the linear dependence of β on ϕ is accounted for by an extra coefficient C_σ on the RHS of equation (5), that has to be of order 1.

The corrected buoyancy or volume force, F_B, is composed of gravity acting on the mass of the bubble,

$$\int_{\mathcal{V}_b} \rho_g \mathbf{g} \, d\mathcal{V} = -\mathcal{V}_b \rho_g \mathbf{g} \mathbf{e}_y \quad (6)$$

and the corrected Archimedes force, F'_B, on an adhering bubble that is calculated by integrating pressure over the entire bubble enveloping area, A_t. This area comprises two parts: one over the water–vapor interface, A_i, and one over the capillary mouth, A_{cap}. This yields:

$$F'_B = \int_{A_i} p_l(y) \, dA + \int_{A_{cap}} p_g \, dA = \int_{A_i} (p_0 + \rho_l g y) \, dA + \int_{A_{cap}} (p_0 + \rho_g g H_0 + 2\sigma/R_{top}) \, dA, \quad (7)$$

in which p_l is the static pressure in the liquid (a function of y), p_0 the static liquid pressure at the bubble top, p_g the vapor pressure inside the bubble and g Earth's gravitational acceleration. H_0 is the vertical distance from capillary to bubble downstream side (bubble top, see Fig. 9). R_{top} is the curvature radius of the bubble top part.

After rearrangement and application of Gauss' integral theorem on the integral over A_i it is found that

$$F'_B = \pi R_c^2 \{(\rho_g - \rho_l) g H_0 + 2\sigma/R_{top}\} \mathbf{e}_x + \rho_l g \mathcal{V}_b \mathbf{e}_y. \quad (8)$$

All these pressure forces are the result of the inner product of static pressure with the outward directed normal vector. Summation of equations (6) and (8) gives for the volume force:

$$\mathbf{F}_B = \left\{(\rho_g - \rho_l) g H_0 + \frac{2\sigma}{R_{top}}\right\} A_{cap} \mathbf{e}_x + \mathcal{V}_b g (\rho_l - \rho_g) \mathbf{e}_y = F_{B,x} \mathbf{e}_x + F_{B,y} \mathbf{e}_y. \quad (9)$$

Expansion force

A growing bubble experiences a dynamic pressure difference over its surface. For an expanding vapor bubble in unbounded liquid this pressure difference is found by applying mass and momentum conservation, giving the well-known Rayleigh equation:

$$\Delta p_{dyn} \propto \rho_l (\tfrac{3}{2}\dot{R}^2 + R\ddot{R}). \quad (10)$$

If the radius R is known as a function of time the resulting expansion force on the bubble is found by integrating equation (10) over the bubble surface. Witze *et al.* [11] did so for a spherical bubble touching a plane surface. They assumed a square-root growth model for the bubble:

$$R(t) = C_g t^{1/2}. \quad (11)$$

The resulting adhering force was found to be

$$F_e = 0.29\pi C_g^4 \rho_l. \quad (12)$$

In a model to predict bubble detachment from a horizontal wall Klausner *et al.* [7] introduce a constant, C_e, in the expansion force:

$$F_e = \pi \rho_l R^2 \{\tfrac{3}{2} C_e \dot{R}^2 + R\ddot{R}\}. \quad (13)$$

C_e accounts for the non-sphericity of the bubble and for the presence of the wall. From a fit with their experimental data they found a value for C_e of 20/3 which is rather large, in view of equation (10). We also adopt equation (13), but shall determine C_e differently. For the growth rate of individual bubbles, a power function with unknown exponent is assumed:

$$R(t) = R_0 + C_\gamma \cdot t^\gamma. \quad (14)$$

From the experiments the values of C_γ and γ of individual bubbles are determined by a least-squares procedure to fit the measured $R(t)$. The values presented in Tables 1 and 2 are values averaged over a number of bubbles per experiment. In the next section, a coefficient fit is done with the individual values of

C_γ and γ (note that R_0 is usually small compared to R_d). To this end, the expansion force is decomposed with the aid of the measured angle Φ:

$$\mathbf{F}_e = F_{e,x}\cos(\Phi)\mathbf{e}_x + F_{e,y}\sin(\Phi)\mathbf{e}_y. \quad (15)$$

Φ is the direction of the bubble midpoint displacement just before detachment. Table 4 lists the mean values of Φ found for some of the steam bubble experiments. The added mass of a bubble growing at a wall is accounted for by the expansion force equation (13).

The drag force on a bubble attached to a wall is, by definition, in the direction of the liquid flow and is written as:

$$F_D = C_{D\frac{1}{2}}\rho_l A V_m^2. \quad (16)$$

C_D is a function of turbulence intensity, bubble Reynolds number and bubble shape. Al-Hayes and Winterton [5] derived a drag coefficient for bubbles attached to the inner side of perspex tubes. For $20 < Re_b < 400$ they found $C_D \approx 1.22$. The bubble Reynolds number in our situation is typically much higher, while flow separation is expected to cause a change in drag coefficient. However, in the next section only forces in the x-direction are considered and equation (16) therefore needs no further evaluation. Interfacial stresses exerted in the x-direction are accounted for by the lift force.

Temperature drop force

In the fluid flowing along the wall a temperature gradient exists due to heat losses through the test section walls. Near the artificial cavity the heating element induces other temperature gradients. The surface tension of pure liquids decreases with increasing temperature. A bubble attached to this cavity has surface tension varying at its interface if the temperature gradients† are not reduced by evaporation or condensation at the interface and the vapor temperature may vary. In pure vapor bubbles with a (nearly) uniform vapor pressure the interface temperature can only vary close to the bubble foot, where thermodynamic nonequilibrium might cause the saturation equation, relating pressure and temperature, not to be valid anymore. The nitrogen bubbles have been injected at isothermal conditions. In this case, there is no surface tension variation nor any other effect due to temperature drop or heat transfer, e.g. through turbulence.

Varying surface tension induces flow in the fluid along the bubble, called thermocapillary or Marangoni flow. Various effects of this flow on bubble growth and detachment have been reported [12, 13]. In the present study it is not claimed that thermocapillarity is important in bubble detachment, although the momentum flux of the liquid jet away from the wall, induced by it, might play a role. The significance of temperature differences near a bubble is merely investigated by attributing a force to it and by trying to find out if it may help to interpret results. In the following, this force is taken to be linear to a typical temperature drop (just as in some Marangoni flows), in order to be able to quantify it. If the temperature drop force would be mainly due to momentum incoming at the bubble base, $\rho_l u_l^2$, caused by evaporation at heat flux $q = \rho_l u_l h$, and if q would be proportional to the temperature drop, ΔT, then the force should be proportional to ΔT^2 rather than ΔT. However, this 'recoil' force is estimated to be six orders of magnitude smaller than other forces.

The sole conclusion to be drawn with the following analysis is whether the temperature drop force is important or not.

An expression for the temperature drop force is derived in the following way. The bubble foot is a circle with radius R_{cap}. Let ΔT denote the mean temperature difference between wall and fluid at the bubble foot and let the surface tension vary linearly with temperature. If the temperature drop force, $F_{\Delta T}$, would be related to thermocapillarity, it can be estimated by:

$$\mathbf{F}_{\Delta T} = 2\pi R_{cap}\frac{\partial\sigma}{\partial T}C_{\Delta T}\Delta T\mathbf{e}_x \quad (17)$$

in which $C_{\Delta T}$ is a coefficient of order 1 and $\partial\sigma/\partial T$ the surface tension temperature gradient. Note that ΔT is a function of liquid velocity and heating rate Q. In Appendix B the following estimate for this function is derived:

$$\Delta T = 0.6 \cdot Q \cdot V_{bulk}^{\xi} \quad (18)$$

with $\xi = -0.568$. The coefficient $C_{\Delta T}$ and exponent ξ will be considered further in the next section.

After initiation and initial rapid growth a bubble expands relatively slowly. Typical growth times for vapor bubbles are in the order of 5 ms. For atmospheric pool boiling in water with 10K superheating, Slooten [14] found the transition from inertial to convective bubble growth to occur at 6 μs after bubble initiation. Our observations yield transition periods of less than 0.3 ms, whereas actual bubble growth always exceeds 1 ms. Since in our study attention is focussed on bubble detachment, the inertial stage and added-mass forces are neglected, except for the $\ddot{R}$-term in equation (13).

The expansion of the bubble induces an acceleration of the fluid. In flow conditions, the interaction of acceleration and vorticity generation at the bubble surface gives rise to the so-called Basset history force. Here this type of force is negligible since both acceleration and vorticity generation are small.

The effect of turbulence is manifesting itself on the time scale of the most energetic eddies in the wall region. The friction velocity, V^*, in our experiments

† It is noted that a temperature gradient is also present at the wall surface in contact with the liquid near the bubble foot. Since solid–fluid interfacial tension is of the order $\sigma\cos\beta$ this temperature gradient also creates tangential stresses, though at places where liquid velocity is zero.

was of the order of 0.03 m s^{-1}. V^* is defined as $\sqrt{\tau_w/\rho_1}$, with τ_w the wall shear stress. Following Klausner *et al.* [7], the most energetic eddies are assumed to have a width λ of about $100\nu/V^*$, with ν the kinematic viscosity of the liquid. The time scale for these eddies is $\tau_{turb} \approx \lambda/V^* \approx 100\nu/(V^*)^2 \approx 3\times10^{-2}$s. Bubble growth time is of the order of 5 ms, smaller than τ_{turb}. Turbulence is therefore neglected. In the next section it is attempted to quantify the unknown coefficients in the forces with the aid of the experimental results of the previous section.

5. ASSESSMENT OF FORCE COEFFICIENTS FROM MEASUREMENTS

In this section, the force balance in the x-direction is constructed with the aid of expressions and coefficients introduced in the previous section. The aim of this study is to quantify coefficients that are connected to the different forces. These coefficients are fitted to our experimental data. A force connected to the temperature difference between wall and fluid is included in the force balance. It is tested whether this force can elucidate the difference in detachment behavior between nitrogen and steam bubbles. Furthermore, it is investigated in Section 5.2 whether a force balance can be used to calculated the bubble detachment radius.

A computer program determines the coefficients of the different forces and calculates statistical quantities of the regression procedure.

5.1. *Analysis and results*

5.1.1. *Approach.* In this section the force balance on a growing bubble in x-direction is studied. The bubble is attached to a capillary and it is assumed that at every moment the force balance $\Sigma_j F_{j,x} = \mathrm{d}(mv_x)/\mathrm{d}t$ holds. The x-components are selected since bubble take-off is in the x-direction (see Fig. 4). The force balance perpendicular to the wall is therefore considered to be more important. Gravity, in addition, dominates in the y-direction, which all but facilitates the determination of the other forces. In addition, if $\beta_a = \beta_r$ (no deviation from a truncated sphere shape, see Fig. 9), immediate detachment occurs according to the balance in the y-direction. Accurate measurement of β_a and β_r would therefore be important in considering the balance, but experimental inaccuracy has been shown to be significant.

The balance in the x-direction reads:

$$F_{\sigma,x}(t)+F_{L_1}(t)+F_{L_2}(t)+F_{\Delta T}(t)+F_{e,x}(t)+F_{B,x}(t)=\frac{\mathrm{d}(mv_x)}{\mathrm{d}t} \quad (19)$$

of the forces of which only the order of magnitude is known. If the expressions for the different forces are copied from Section 4, the force balance gets the following form:

$$\begin{aligned}\frac{\mathrm{d}(mv_x)}{\mathrm{d}t} &= -C_\sigma\cdot R_{cap}\sigma\int_0^{2\pi}\sin\beta(\phi)\mathrm{d}\phi \\ &+C_{L_1}A_2^1\rho_1 V_m^2+C_{L_2}\rho_1\dot{V}_b V_m\frac{\mathrm{d}V_m}{\mathrm{d}_x} \\ &+2\pi R_{cap}\frac{\partial\sigma}{\partial T}C_{\Delta T}\cdot 0.6\cdot Q\cdot V_{bulk}^{\xi} \\ &+\pi\rho_1 R^2\{\tfrac{3}{2}C_e\dot{R}^2+R\ddot{R}\}\cos(\Phi) \\ &+\left\{(\rho_g-\rho_1)gH_0+\frac{2\sigma}{R_{top}}\right\}A_{cap}. \end{aligned} \quad (20)$$

Note that the added mass is accounted for by the second-last term in equation (20), the expansion force F_e. The direction of the coordinate axes is depicted in Fig. 9. In the acceleration term above, $\mathrm{d}(mv_x)/\mathrm{d}t$, v_x is the bubble center of mass velocity and m the bubble mass. For this term the following estimate is made:

$$\begin{aligned}\frac{\mathrm{d}(mv_x)}{\mathrm{d}t} &= \rho_g\left(v\frac{\mathrm{d}\dot{V}_b}{\mathrm{d}t}+\dot{V}_b\frac{\mathrm{d}v}{\mathrm{d}t}\right) \\ &\approx \rho_g(4\pi v R^2\dot{R}+4/3\pi R^3\frac{\mathrm{d}v}{\mathrm{d}t}\Big) \\ &\approx 4/3\pi\rho_g R^2(3\dot{R}^2+R\ddot{R}) \approx 4/3\frac{\rho_g}{\rho_1}F_e \end{aligned} \quad (21)$$

with C_e in equation (20) of order 1. The factor ρ_g/ρ_1 demonstrates that the acceleration force is three orders of magnitude less than F_e. The acceleration force contribution, being less than the error in C_e, is therefore neglected in the following.

The force balance in equation (20) is rewritten in terms of the coefficients to be fitted and the remaining parts:

$$0 = C_e X_e(n)+C_\sigma X_\sigma(n)+C_{L_1}X_{L_1}(n)+C_{L_2}X_{L_2}(n)+C_{\Delta T}X_{\Delta T}(\xi,n)+X_z(n) \quad (22)$$

where X_z contains the terms without a coefficient and n numbers the data points. For each bubble measured, certain instants of time before detachment are selected and each time yields a data point, since equation (20) should hold at all times. X_z contains the following quantities measured:

$$X_z = \pi\rho_1 R^3\ddot{R}\cos(\Phi)+\left\{(\rho_g-\rho_1)gH_0+\frac{2\sigma}{R_{top}}\right\}A_c. \quad (23)$$

To circumvent difficulties in the determination of bubble shapes and related quantities, such as $\ddot{R}$, a restriction on the set of possible bubble shapes is made. In the present model the bubble is assumed to have the shape of a truncated sphere (see Fig. 9). The asymmetry of the bubble is only accounted for by including the measured upstream and downstream contact angles β_a and β_r, respectively. The contact angles at intermediate circumferential angle ϕ are lin-

Table 5. Bubble sets used in the coefficient determination

Set no.	Number of bubbles	Type	V_{bulk}	D_{cap} (μm)
1	6	N_2	$=0$	101
2	2	N_2	$=0$	132
3	10	N_2	$\neq 0$	101
4	25	N_2	$\neq 0$	132
5	30	steam	$\neq 0$	130

Table 6. Results for the force balance minimization procedure on data sets 1 and 2. Nitrogen bubbles with zero bulk liquid speed

Data set	Fixed coefficients	Resulting values	$\|\overline{F_n}\|$ (μN)
1	$C_{L_1}=0$ $C_{L_2}=0$ $C_{\Delta T}=0$	$C_e=0.6\pm0.1$ $C_\sigma=0.6+0.2$	0.49
2		$C_e=0.6\pm0.1$ $C_\sigma=0.6\pm0.4$	0.49

early interpolated from β_a to β_r. The bubble growth rate coefficient C_γ and the growth rate exponent γ [see equation (14)] are determined for all bubbles individually by fitting, and used to compute $\dot{R}$ and $\ddot{R}$ at the instants of time selected. In this way, the uncertainty in individual measurements is suppressed. A similar procedure is applied to β_a and β_r.

The force balance equation (19) depends on time and on the coefficients C_σ, C_{L_1}, C_{L_2}, $C_{\Delta T}$ and C_e. Estimates for these coefficients are found by a procedure based on strict application of the total force balance equation (19). At every instant of time the force balance for every bubble from each capillary is made to be nearly satisfied by an appropriate selection of the coefficients C. The way this is done is explained in the next section.

5.1.2. *Procedure and results.* The results from experiments on steam and nitrogen gas bubbles are divided into different data sets, in order to increase the accuracy by reducing the number of coefficients to be fit. Table 5 lists the sets. The division is made according to type of bubble (nitrogen or steam), zero or non-zero liquid bulk velocity and capillary radius. The coefficients, fitted to the data of each set, are presented in Tables 6–8. The tables list the data set(s) used, the value of coefficients held fixed and the results for the unknown coefficients. The residuals obtained by computing the right-hand-side of equation (22) with the fitted coefficients are averaged over all data of a data set to yield $|\overline{F_n}|$.

The first two data sets comprise the nitrogen experiments with zero bulk liquid speed (eight bubbles). With no liquid flowing past the bubble and no additional heating of the wall only buoyancy, the expansion force and surface tension act on the bubble. The correlation coefficient between the input data for the combined data sets is very high (0.99). The scatter plot in Fig. 10 illustrates why the correlation is high. In this figure the X_e-values of the data points are plotted vs their X_σ-values. The data of set 2 are in the lower left corner, while the other data are grouped in the opposite corner. This grouping leads to a high correlation coefficient. Keeping the two data sets apart leads to lower correlation coefficients. This yields the average values $C_e = 0.6\pm0.1$ and $C_\sigma = 0.6\pm0.2$, see Table 6. Both coefficients are of order 1, indicating that the minimization procedure yields realistic values. The error indicated is the estimate for the standard deviation, given by the square root of the diagonal elements of the error matrix.

Figure 11 depicts the residual force on the bubbles from data sets 1 and 2, by using the C_e and C_σ values of Table 6. This force decreases monotonely as a function of time for each bubble (each line segment in Fig. 11). This is due to the fact that parameters, such as C_γ, are constant in time, as explained above.

Next, experiments with nitrogen and non-zero liquid speeds are used to determine the lift coefficients C_{L_1} and C_{L_2}, see Table 7. The value of the coefficient for the 'vorticity' lift force, C_{L_2}, tends to the lowest value possible (set to 10^{-6}), while its deviation is substantially higher. Hence, it is allowed statistically to take C_{L_2} equal to zero. The functions X_{L_1} and X_{L_2} of equation (22), which are connected to the lift coefficients, have a rather large correlation coefficient of 0.89. In Fig. 12, the scatter plot for the X_{L_2} values vs X_{L_1} for sets 3 and 4 is given. With sets 1 and 2 better results have been obtained above by splitting into two separate sets. This does not work for sets 3 and 4. That X_{L_1} and X_{L_2} are correlated implies that it is better to determine only C_{L_1} while keeping C_{L_2} fixed, or vice-versa. If the theoretical estimate of 11/8 for C_{L_1} is fixed, the value of 0.1 for C_{L_2} is found. All results are summarized in Table 7. The two cases, $C_{L_2}=0$ and $C_{L_1}=11/8$ are considered to be limiting cases and are both analyzed in the following.

Set number 5, containing data of 30 boiling bubbles, is used to examine the importance of the force connected to the local heating of the wall by the bubble generator (see Table 8). This force might be helpful in explaining the different angle of detachment and other differences between nitrogen and vapor bubbles, as discussed above. In two runs listed in Table 8, the exponent ξ is set to -0.6, which is the value resulting from the model of Appendix B. It is noted that $C_{\Delta T}$ should be of order 1. If C_{L_2} is set to zero, a very small value of $C_{\Delta T}$ results, with a large uncertainty. If C_{L_1} is set to 11/8, $C_{\Delta T}$ is found to be 0.9. This is a result of the expected order of magnitude. The low value of $C_{\Delta T}$ for $C_{L_2}=0$ might be due to the rather high correlation (0.57) between the X_{L_1} and $X_{\Delta T}$ parameters.†

† The correlation coefficient between X_{L_2} and $X_{\Delta T}$ is 0.01.

Table 7. Values for fixed coefficients and estimated coefficients for nitrogen bubbles with non-zero bulk liquid speed, data sets 3 and 4

Data set	Fixed coefficients		Resulting values	$\lvert\overline{F_n}\rvert$ (μN)
3 and 4	$C_e = 0.6$		$C_{L_1} = 1.9 \pm 0.2$	7.0
			$C_{L_2} = 10^{-5} \pm 0.05$	
	$C_\sigma = 0.6$	$C_{L_2} = 0.0$	$C_{L_1} = 1.83 \pm 0.05$	7.0
		$C_{L_1} = 11/8$	$C_{L_2} = 0.1 \pm 0.01$	7.5

Table 8. Results for coefficient fit with steam bubbles

Data set	Fixed coefficients		Resulting values	$\lvert\overline{F_n}\rvert$ (μN)
5	$C_e = 0.6$	$C_{L_1} = 1.83$ $\xi = -0.6$	$C_{\Delta T} = 6 \times 10^{-4} \pm 0.4$	1.4
		$C_{L_2} = 0.0$	$\xi = 4 \pm 10^6$, $C_{\Delta T} = 5 \times 10^{-6} \pm 14$	1.39
	$C_\sigma = 0.6$	$C_{L_1} = 11/8$ $\xi = -0.6$	$C_{\Delta T} = 0.9 \pm 0.3$	1.2
		$C_{L_2} = 0.1$	$\xi = -5$, $C_{\Delta T} = 0.2 \pm 0.2$	0.8

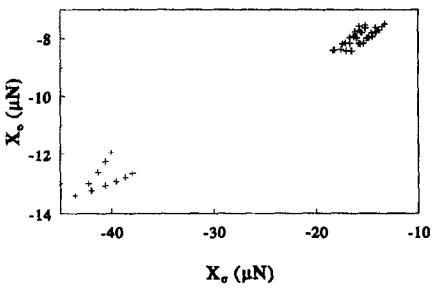

Fig. 10. X_e vs X_σ-values of the data points from sets 1 and 2.

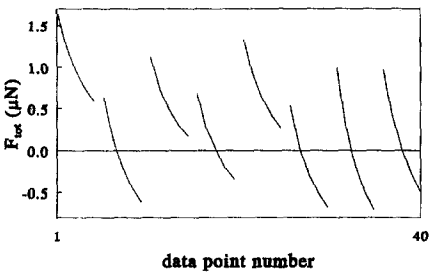

Fig. 11 Total force on the bubbles of sets 1 and 2. Values computed with $C_e = 0.6$ and $C_L = 0.6$.

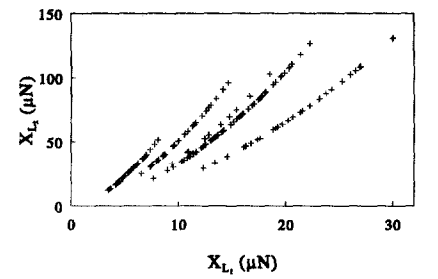

Fig. 12. X_{L_2}- vs X_{L_1}-values of data in sets 3 and 4.

Data set 5 has also been analyzed by varying both $C_{\Delta T}$ and the exponent ξ in $F_{\Delta T}$, making the fitting model non-linear. Although the residuals $\lvert\overline{F_n}\rvert$ are smaller than with ξ fixed, the uncertainty of $C_{\Delta T}$ at the lower C_{L_2}-value is only increased, whereas the ξ-value of the higher C_{L_2}-value (0.1) is the preset minimum, i.e. -5. This makes it clear that the data do not favor the determination of ξ.

5.1.3. *Discussion.* From the nitrogen bubble experiments with no bulk liquid speed it is found that C_e and C_σ have a value of 0.6 ± 0.1 and 0.6 ± 0.2, respectively. A better accuracy can only be achieved by more data and by improved knowledge of the local contact angles β_a and β_r.

The description of both lift forces F_{L_1} and F_{L_2} leads to data sets that are more or less correlated. Attributing a lower value to F_{L_1} leads to a higher value of F_{L_2} and vice versa. By considering realistic extremes, C_{L_1} is found to be 1.8 ± 0.2 approximately, and C_{L_2} to be 0.1 or less. These values do not exclude the possibility that a lift force of the type F_{L_2}, see equation (3), is not active at all, so it is recommended to perform dedicated experiments in which the lift force is isolated, in order to increase accuracy.

According to the estimates of Appendix B, the action of the temperature drop force would result in ξ having a value of -0.6, approximately. With this value of ξ, and with C_{L_1} fixed to 11/8, the coefficient found for this force is $C_{\Delta T} = 0.9 \pm 0.3$, implying that an extra detaching force should be present in the case of water vapor bubbles. The results are not conclusive, however, since there is a dependency on C_{L_2} and the value of C_{L_2} is not yet quantified accurately enough. It is clear that either F_{L_2} is not active at all, i.e. $C_{L_2} = 0$ and F_{L_1} is relatively large, or $C_{\Delta T}$ has a significant value. It can not be decided on basis of the present data which option corresponds to reality, but both options are equally interesting. The authors have a tendency to fancy the '$C_{\Delta T}$ significant' option,

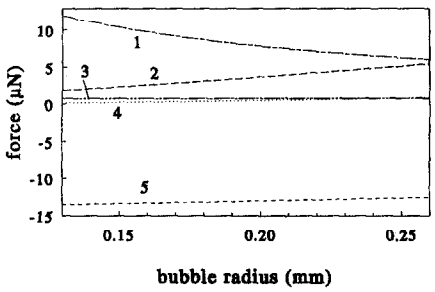

Fig. 13. The computed individual forces on a vapor bubble from set 5. Values for coefficients listed in third line of Table 8 are used. (1) $F_{B,x}$; (2) F_{L_1}; (3) $F_{\Delta T}$; (4) F_{L_2}; (5) $F_{\sigma,x}$.

because of the correlation coefficient (see above) and the observed differences between detaching vapor and nitrogen bubbles.

With $C_{L_2} = 0.1$ and $C_{\Delta T} = 0.9$ the values of the individual forces as a function of the bubble radius are given in Fig. 13. Especially for small bubble radii, both lift forces, F_{L_1} and F_{L_2} are of minor importance. The vorticity lift force, F_{L_2}, and the temperature drop force, $F_{\Delta T}$, are of minor importance during the whole of the bubble growth. The expansion force, F_e, is even smaller and is therefore not depicted. The low relative importances of F_{L_2} and $F_{\Delta T}$ explain why it is difficult to establish their absolute value on the basis of experiments with detaching bubbles.

5.2. *Prediction of detachment radius*

Crucial in predicting the detachment radius is the detaching criterion. Mostly this criterion was formulated [4, 5, 7, 8] in terms of the net force on the bubble: as soon as the net force is pointing away from the wall the bubble would take off. However, if all forces are correctly included in a force balance, the sum of these forces should be zero at all times. Note that the method of analysis of the previous section is based on this observation.

Let us now try to devise a practical detachment criterion in much the same way it was done by others before. A typical value of the standard deviation of the residual force F_n is 2 μN. The criterion for bubble detachment is tentatively formulated as follows: a bubble is supposed to detach if F_n, as given by the RHS of equation (22), exceeds 2 μN. The force balance equation (20) is based on some assumptions, one of them being that the bubble shape is a truncated sphere. If the residual force, F_n, exceeds a threshold, this assumption is, according to the criterion, not valid anymore and detachment occurs.

This criterion has been applied to the 30 steam bubbles from the fifth set, with the result that 29 of the 30 bubbles were found not to detach, since the residual force always exceeded the threshold value or remained negative. After increasing the threshold value to 10 μN, seven bubbles did detach. The differences between calculated and measured values were, however, very large and nearly all were outside the $\pm 50\%$ range. It is therefore concluded that prediction of bubble detachment diameters with a criterion like the one above is unsatisfactory, despite the fact that this was quite often done in the past [4, 5, 7, 8]. The geometrical criterion of Chesters [15] would do better, since it is based on the (im)possibility of fitting interface shapes to the cavity mouth. This criterion, however, does not explain the actual forces involved.

What seems to be missing is knowledge of the forces that actually cause a liquid bridging over the cavity mouth, i.e. that cause detachment of a bubble. If the physics involved were fully understood, an appropriate detachment criterion could be devised.

6. CONCLUSIONS

Forces acting on bubbles attached to a capillary are to some degree of accuracy quantified with the aid of a fitting procedure and a step-by-step approach with results of three types of experiments. Two types of experiments have been with nitrogen injection from capillaries of 100 and 132 μm diameter. The other experiments have been with boiling bubbles, generated by local heating of a 130 μm diameter capillary.

The surface tension force coefficient C_σ, as defined in equation (20), is found to satisfy $0.4 \leqslant C_\sigma \leqslant 0.8$. These are considered to be realistic values; the spread is attributed mainly to uncertainties in the values of the contact angles β_a and β_r. The expansion force coefficient, C_e, is found to be 0.6 ± 0.1. This is less than the value found by Klausner *et al.* [7], but is considered to be more realistic since their value is much larger than the value for a bubble, expanding freely far from a wall. Two lift forces are analyzed: one a contribution of uniform flow described by potential theory, F_{L_1}, and the other due to the vorticity, F_{L_2}. The data sets for the two lift forces are found to be more or less correlated. Either C_{L_1} or C_{L_2} has therefore been fixed in the fitting procedure, to the theoretical value 11/8 and to 0, respectively. The option $C_{L_2} = 0$ is selected on basis of a fit without fixed coefficients; this yields $C_{L_1} = 1.83$ in the fitting procedure, which is close to 11/8. The option $C_{L_1} = 11/8$ yields $C_{L_2} = 0.1$, which is still small. These findings suggest that the relation for a vorticity lift force, as described by Auton [1], may not be applicable to detaching bubbles with flow along a wall. Dedicated measurements of lift forces are required to settle this question.

The detachment radii of nitrogen bubbles and steam bubbles are found to be different under similar circumstances. Also the angle of the trajectory of a detaching bubble with the vertical wall is different for nitrogen and steam bubbles. These differences may be due to the action of a force connected to the local heating of the wall. An expression for this force is given by equation (17). For the temperature drop ΔT in this equation, a numerical analysis has yielded equation (18). Coefficient fits yield that either $F_{L_2} = 0$ or the temperature drop force is significant, i.e. $C_{\Delta T} = 0.9$. If $C_{L_2} = 0$ the temperature drop force

probably is of minor importance. To reach fully conclusive results, knowledge of the lift forces would have to be improved. As yet, the authors believe that the option $C_{L_1} = 11/8, C_{L_2} = 0.1$ and $C_{\Delta T} = 0.9$ is more realistic in view of the discrepancies observed between nitrogen and steam bubbles and for other reasons explained above.

It is shown that if a force balance like equation (20) is used to predict detachment radii, the prediction is unsatisfactory. The authors believe that such a prediction criterion lacks some of the physics involved. Its use is not recommended, despite its manifold occurrence in literature [4, 5, 7, 8].

REFERENCES

1. T. R. Auton, The dynamics of bubbles, drops and particles in motion in liquids. Ph.D. Thesis, University of Cambridge (1983).
2. R. Siegel, Effects of reduced gravity on heat transfer. In *Advances in Heat Transfer* (Edited by S. P. Hartnett), Vol. 4. Academic Press, London (1967).
3. M. G. Cooper and T. T. Chandratilleke, Growth of diffusion-controlled vapour bubbles at a wall in a known temperature gradient, *Int. J. Heat Mass Transfer* **24**(9), 1475–1492 (1981).
4. N. Koumoutsos, R. Moissis and A. Spiridonos, A study of bubble departure in forced-convection boiling, *J. Heat Transfer Trans. ASME*, 223–230 (1968).
5. R. A. M. Al-Hayes and R. H. S. Winterton, Bubble diameter on detachment in flowing liquids, *Int. J. Heat Mass Transfer* **24**, 223–230 (1981).
6. M. G. Cooper, K. Mori and C. R. Stone, Behaviour of vapour bubbles growing at a wall with forced convection, *Int. J. Heat Mass Transfer* **26**(10), 1489–1507 (1983).
7. J. F. Klausner, R. Mei, D. M. Bernard and L. Z. Zeng, Vapor bubble departure in forced convection boiling, *Int. J. Heat Mass Transfer* **36**(3), 651–661 (1993).
8. L. Z. Zeng, J. F. Klausner, D. M. Bernhard and R. Mei, A unified model for the prediction of bubble detachment diameters in boiling systems—II, flow boiling, *Int. J. Heat Mass Transfer* **36**(9), 2271–2279 (1993).
9. P. G. Saffman, The lift on a small sphere in a slow shear flow, *J. Fluid Mech.* **22**(2), 385–400 (1965).
10. A. Melling and J. H. Whitelaw, Turbulent flow in a rectangular duct, *J. Fluid Mech.* **78**(2), 289–315 (1976).
11. C. P. Witze, V. E. Schrock and P. L. Chambre, Flow about a growing sphere in contact with a plane surface, *Int. J. Heat Mass Transfer* **11** 1637–1652 (1968).
12. E. S. Gaddis, The effect of liquid motion induced by phase change and thermocapillarity on the thermal equilibrium of a vapour bubble, *Int. J. Heat Mass Transfer* **15** 2241–2250 (1972).
13. Y. S. Kao and D. B. R. Kenning, Thermocapillary flow near a hemispherical bubble, *J. Fluid Mech.* **53**(4), 715–735 (1972).
14. P. C. Slooten, Departure of vapor and gas bubbles in a wide pressure range. Ph.D. Thesis, Eindhoven University of Technology (1984).
15. A. K. Chesters, An analytical solution for the profile and volume of a small drop or bubble symmetrical about a vertical axis, *J. Fluid Mech.* **81**(4), 609–624 (1977).
16. Richard W. Miller, *Flow Measurement Handbook* (2nd Edn). McGraw-Hill, New York (1989).

APPENDIX A. LIFT COEFFICIENT ON A HEMISPHERE IN POTENTIAL FLOW

The 'Bernoulli suction' lift coefficient C_{L_1}, as introduced in equation (3), is derived in the following way. Suppose a potential flow along a sphere as depicted in Fig. A1. Far away from the sphere the flow is parallel in $+x$-direction, in the vicinity it is described by the flow around a dipole in the origin. The radius of the sphere is unity. The relations between Cartesian and spherical coordinates are:

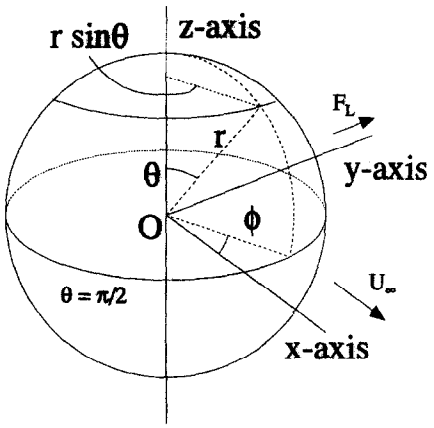

Fig. A1. Spherical polar coordinate system used to calculate lift force on hemisphere.

$$x = r\sin(\theta)\cos(\phi)$$
$$y = r\sin(\theta)\sin(\phi)$$
$$z = r\cos(\theta). \tag{A1}$$

If U_∞ is the undisturbed fluid speed in the x-direction, the stream function, Ψ, is given by:

$$\Psi = \tfrac{1}{2}U_\infty \sin^2(\theta)\left(r^2 - \frac{1}{r}\right). \tag{A2}$$

On the surface of the sphere the radial velocity is zero, while the tangential velocity is given by

$$u_\theta = \tfrac{3}{2}U_\infty \sin(\theta). \tag{A3}$$

The lift force on the hemisphere with $y \geqslant 0$ is found by integrating the pressure at the surface over the whole area. The pressure is found by application of Bernoulli's law:

$$p - p_\infty = \tfrac{1}{2}\rho_1\{u_\theta^2 - U_\infty^2\} = \tfrac{1}{2}\rho_1 U_\infty^2\{\tfrac{9}{4}\sin^2(\theta) - 1\}. \tag{A4}$$

By definition,

$$C_{L_1} = \frac{F_L}{\tfrac{1}{2}\rho_1 A U_\infty^2}. \tag{A5}$$

As A is the area of the body cross section perpendicular to the flow direction, $A = \frac{1}{2}\pi$. The lift force acts in the y-direction, therefore the inner product of the normal vector at the hemisphere surface and the unit y-vector has to be incorporated in the integration, giving:

$$C_{L_1} = \frac{2}{\pi}\int_0^\pi \sin(\phi)\,d\phi \int_0^\pi \sin^2(\theta)\{\tfrac{9}{4}\sin^2(\theta) - 1\}\,d\theta$$
$$= \frac{4}{\pi}\{\tfrac{9}{4}\cdot\tfrac{3}{8}\pi - \tfrac{1}{2}\pi\} = \tfrac{11}{8}. \tag{A6}$$

APPENDIX B. ESTIMATE FOR THE DEPENDENCE OF THE TEMPERATURE DROP FORCE ON LIQUID SPEED

As the water is heated around the cavity, liquid temperature gradients occur near the foot of the bubble. If water

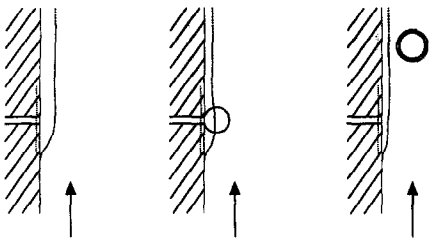

Fig. B1. Temperature boundary layer generated by local heating of the wall. The heated area is indicated by the dotted line in the wall. Left: fully developed. Middle: decrease of boundary layer thickness by heat consumption of growing bubble. Right: reduced thickness after bubble detachment.

is flowing past the bubble the temperature at the bubble foot will vary slightly along the bubble foot. In order to appreciate the importance of the temperature drop force, the water superheating at the foot, ΔT, has to be modeled as a function of bulk liquid speed, V_{bulk}, and heating rate Q. A two-dimensional geometry is assumed. This approximation should hold near the upstream end of the bubble. At other places, fluid motion is also directed towards the bubble foot, which to some extent validates the two-dimensional assumption.

The superheating ΔT at the bubble foot depends on time. Before initiation of bubble growth, heat is accumulated in the wall and also in the liquid in which a temperature boundary layer develops (see Fig. B1). In the following calculation, the temperature boundary layer is assumed to be fully developed and stationary (left drawing). In the other drawings, the effect of a bubble on this layer is depicted. The bubble takes up heat from the wall, giving the boundary layer less time to develop. The thinner layer results in a larger temperature drop along the bubble surface. For larger bubbles this temperature drop is less since detachment frequency is lower and there is more time for the layer to develop. This leads to increasing temperature drop with increasing liquid speed (and decreasing detachment radii).

The temperature distribution in the boundary layer is governed by the stationary convection–diffusion equation:

$$-\alpha\nabla^2\theta + V\frac{\partial\theta}{\partial y} = \frac{Q(x,y)}{\rho_s c T_\infty} \tag{B1}$$

where α is the thermal diffusivity, different for wall and fluid, ρ_s the mass density of the (solid) wall, c the heat capacity of the wall and θ the dimensionless temperature defined by

$$\theta = (T - T_\infty)/T_\infty \tag{B2}$$

with T_∞ the upstream (saturation) temperature.

Q is the heat production rate of the source (in J m^{-3} s^{-1}), distributed uniformly over a square region around $(-q, 0)$. The sides of this region have length q. The two-dimensional geometry is given in Fig. B2. The y-axis (see Fig. B2) is the boundary between wall and fluid.

The velocity profile of the saturated liquid is that of a turbulent flow in a channel with square cross section and a channel Reynolds number between 1×10^4 and 6×10^4. An estimate for the time-averaged velocity at the cross section where the cavity is located is taken from the measurements of Melling and Whitelaw [10]. From their experiments at $Re = 4.2 \times 10^4$ the following relation between axial velocity and position in the channel is derived:

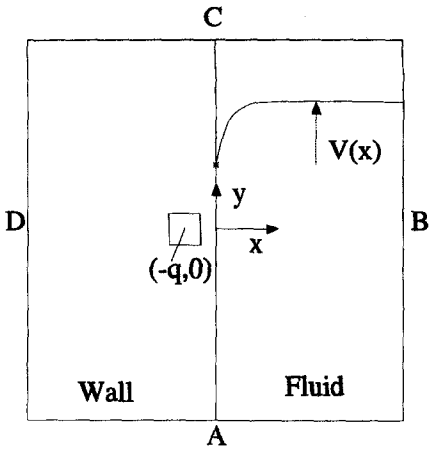

Fig. B2. Geometry used in calculation of liquid temperature distribution caused by a square heat source around $(-q, 0)$ and given liquid velocity distribution.

$$V = V_s\left(\frac{x}{l}\right)^{1/n} \tag{B3}$$

with l half the channel diameter, V_s the liquid speed at the channel centre; $V_s \approx 1.25 V_{bulk}$, V_{bulk} being the liquid bulk speed. Coordinate x represents the distance from the wall ($0 \leqslant x \leqslant l$). Melling and Whitelaw [10] measured $n = 5.36$ for $Re = 4.2 \times 10^4$. For other Reynolds numbers, a logarithmic dependence of n on Re as in circular pipes (see for instance ref. [16]), is assumed:

$$n = 0{,}503 \ln(Re) \tag{B4}$$

ln is the natural logarithm.

The temperature boundary layer generated by the heat source embedded in the wall is calculated with boundary conditions $\theta = 0$ at boundaries A and B (see Fig. B2), while at C and D the normal heat flux is zero, i.e. $\partial\theta/\partial n = 0$, with n the normal to the wall. The solution is obtained with a finite element package with a mesh refined in regions with high temperature gradients. Upwind differencing is used to effectively handle the convective heat transport. It is found that the temperature boundary layer thickness only marginally decreases with increasing liquid bulk speed at constant heating rate.

The difference in temperature of position (0,0), the bubble generation site, and the liquid bulk is calculated for eight mean liquid velocities between 0.05 and 1.0 m s^{-1}. The heating power, Q, of the bubble generator was set to the typical value of 10 W m^{-3}. For the wall the material properties of glass were used (type I bubble generator), for the liquid the properties of water at saturation temperature at atmospheric pressure.

The calculated results for ΔT are very well represented by a power function:

$$\Delta T = 0.6 \cdot Q \cdot V_{bulk}^{\xi} \tag{B5}$$

with $\xi = -0.568$, V_{bulk} in m s^{-1}, and Q in W m^{-3}. This equation is equation (18). Because equation (30) is linear in θ, an increase in heating power leads to a proportional increase in ΔT, as has been made explicit by the factor Q in the above equation. Expression (B5) is used in equation (17) to give $F_{\Delta T}$.